

Research Article

Influence of the Hydraulic Boundary Condition between the Embankment and Saturated Half-Space on the Train-Induced Ground Vibration

Zong-hao Yuan,¹ Zhi-gang Cao ,² Hao Tang,² and Si Sun²

¹College of Civil Engineering and Architecture, Zhejiang University of Technology, Hangzhou 310014, China

²Research Center of Coastal and Urban Geotechnical Engineering, Department of Civil Engineering and Architecture, Zhejiang University, Hangzhou 310027, China

Correspondence should be addressed to Zhi-gang Cao; caozhigang2011@zju.edu.cn

Received 13 December 2018; Accepted 31 January 2019; Published 11 February 2019

Academic Editor: Gaetano Giunta

Copyright © 2019 Zong-hao Yuan et al. This is an open access article distributed under the Creative Commons Attribution License, which permits unrestricted use, distribution, and reproduction in any medium, provided the original work is properly cited.

A three-dimensional analytical model was proposed to investigate the influence of the hydraulic boundary of the ground surface on the train-induced ground vibrations. The ground was simulated as a fully saturated poroelastic half-space and the embankment as a rectangular elastic soil layer with finite width. The rails and the sleepers were modeled as Euler beams and a Kirchhoff plate, respectively. Two hydraulic boundaries of the interface between the embankment and the ground surface were simplified as two limiting cases, namely, the permeable and impermeable cases. The linearized dynamic equations of motion for the fully saturated poroelastic soil and the elastic embankment were solved by Fourier transform and Fourier series. The vertical velocity and pore pressure were firstly calculated in the frequency-wavenumber domain and then transformed into the time-space domain by inverse Fourier transform. The influence of the hydraulic boundary at the ground surface on the train-induced ground vibration was specially investigated. It was found that the hydraulic boundary condition has a significant influence on ground-borne vibrations for the high-speed moving train with high load excitation frequencies.

1. Introduction

The high-speed trains usually cause disturbance to residents and detrimental effects on the buildings nearby. In the past decades, researchers have made a lot of efforts to investigate the dynamic response of the ground generated by moving traffic loads.

Some researchers [1–3] have established several three-dimensional models to study the dynamic response of a homogeneous elastic half-space due to the moving constant load applied on the ground surface. In order to include the track, Metrikine and Dieterman [4] and Kim [5, 6] investigated the dynamic interaction between an Euler beam and the underlying elastic half-space, and it was found that resonance phenomenon occurs when the moving load velocity approaches the critical velocity of the beam-soil model. Sun [7] presented a theoretical three-dimensional model to simulate the vibrations of a rigid pavement resting

on an elastic half-space subjected to a moving point load for the subsonic, transonic, and supersonic speed, respectively. Using a simplified formulation of the railway track, namely, a layered beam structure resting on a layered elastic ground, Sheng et al. [8–10] proposed a series of analytical models to study the ground vibrations by solving the wave equations for the Euler beam and the viscoelastic half-space.

All the works mentioned above treated the soil as a single-phase elastic and viscoelastic medium. However, underground water usually exists, which leads to the fact that the soil is saturated with water and becomes a two-phase material. For the two-phase medium, the coupling effects between the soil skeleton and the pore-fluid cannot be neglected when subjected to moving train loads [11]. If the half-space is modeled as a saturated poroelastic medium by using Biot theory [12], the pore-fluid related parameters and hydraulic boundary conditions can be considered. By neglecting the coupling between the soil skeleton and the

fluid, Siddharthan et al. [13] solved Biot equations of $\mathbf{u-p}$ formulation under the plane strain condition, and the displacement and pore pressure responses caused by the moving load with a low velocity were given. Based on Siddharthan work, Theodorakopoulo et al. [14] and Theodorakopoulo [15] solved the complete $\mathbf{u-w-p}$ equation and presented a two-dimensional model to study the dynamic responses of the saturated soil under rectangular moving loads. Jin [16] established a three-dimensional model to calculate the dynamic response of the saturated soil for the case of a point load moving on the ground surface. By adopting four scalar potential functions and Helmholtz decomposition theorem, Liu et al. [17] studied the dynamic response of saturated soil to a harmonic moving load under conditions of plane strain. Xu et al. [18] researched the vibrations of the infinite Euler beam on a multilayered saturated half-space induced by moving loads on the beam, in which the effects of soil properties and the load velocity were studied. Gao et al. [19, 20] presented a track-ground interaction model to evaluate the train-induced vibration in the saturated ground. The influence of permeability coefficient and shear wave velocity on the attenuation of ground vibration was analyzed in detail. Chahour et al. [21] carried out a spectral analysis of a railway track coupled to the multilayered poroelastic half-space for the case of a moving harmonic load moving on the rails. However, in the above works the stress boundary condition between the beam and the underlying half-space was simplified as uniform stress distribution in the transverse direction, and the displacement compatibility condition is only valid at the center line of the track, which could not model the real dynamic interaction between the railway track and the ground precisely when subjected to high frequency loads. Based on Biot's theory, Cai et al. [22] and Cao et al. [23] established a track-embankment-soil model with continuous displacement and stress compatibility conditions at the track-ground interface to investigate the ground vibration induced by a moving train.

It should be noted that a fully permeable boundary condition is usually assumed at the ground surface or between the track structure and underlying half-space in the above studies. However the hydraulic boundary condition between the track-embankment and ground may deteriorate during the service time due to the breakage of road bed filling particles; thus the contact surface between the track and half-space is actually partially permeable. The partially permeable interface between the embankment and ground and the fully permeable free ground surface leads to a mixed boundary value problem, which is not easy to be solved analytically. To circumvent the difficulty of the mixed boundary value problem, two limiting cases, namely, fully permeable and fully impermeable ground surface, were used to bound the actual hydraulic boundary condition. A study by Zhou et al. [24] showed that the dynamic response of a saturated half-space for the permeable and impermeable ground surface exhibits an obvious difference; however the dynamic interaction between the track system and the ground was not considered in this study. To date, few studies focus on the effects of the hydraulic boundary condition on the train-induced ground vibration. In order to make accurate prediction of

train-induced vibrations, the effect of the hydraulic boundary condition on the train-induced ground vibration needs to be investigated.

In the present paper, the effects of the hydraulic boundary condition between the embankment and the saturated half-space on the train-induced ground vibrations are investigated by a three-dimensional semianalytical model. The model consists of rails, sleepers, an embankment, and a half-space which are simulated as Euler beams, a Kirchhoff plate, an elastic layer, and a poroelastic soil medium, respectively. By using Fourier transform and Fourier series techniques, the linearized dynamic equations of motion for the embankment and fully saturated poroelastic half-space were solved in the frequency-wavenumber domain. The critical velocity of the embankment-ground structure under different hydraulic boundary conditions was investigated. The effects of the hydraulic boundary condition on the dynamic responses of the ground generated by the moving trains with different self-excitation frequencies were analyzed.

2. Governing Equations and Solutions

2.1. Governing Equations. A detailed track-embankment-ground model is shown in Figure 1, consisting of a half-space, an embankment, sleepers, and two rails. The embankment is modeled as a rectangular elastic layer with finite width $2a_e$ and finite thickness d which is resting on a homogeneous poroelastic half-space. The sleeper and rails are simulated as a Kirchhoff plate and Euler-Bernoulli beams. A high-speed train with 5 carriages is used to simulate the moving train loads and the detailed load amplitude and geometric distribution are presented in Figure 2. The drainage condition of interface between the embankment and the ground usually deteriorates during the service period due to the particle breakage and the invasion of fines. Thus, the interface is actually partially impermeable; then the hydraulic boundary of the ground surface becomes a mixed boundary with the partially permeable interface and the permeable free surface. In order to facilitate the analytical solutions of this model, two limiting cases, namely, the permeable and impermeable ground surface, are considered in the present study to bound the effects of the hydraulic boundary at the ground surface.

The Lamé equations of the embankment layer are given as [27]

$$(\lambda_e + 2\mu_e) \nabla (\nabla \cdot \mathbf{u}_e) - \mu_e \nabla \times (\nabla \times \mathbf{u}_e) = \rho_e \ddot{\mathbf{u}}_e \quad (1)$$

where the subscript e denotes the embankment and the dot over the variable represents the derivative with respect to time t . $\mathbf{u}_e = \{u_e, v_e, w_e\}$ is the displacement vector and λ_e, μ_e are Lamé constants of the elastic layer.

The traction on a plane with the normal direction \mathbf{e}_k ($k=x, y, z$) is expressed as

$$\boldsymbol{\sigma}_e^{(e_k)} = \lambda_e \mathbf{e}_k \nabla \cdot \mathbf{u}_e + 2\mu_e \partial_k \mathbf{u}_e + \mu_e \mathbf{e}_k \times (\nabla \times \mathbf{u}_e) \quad (2)$$

where $\nabla = \{\partial_x, \partial_y, \partial_z\}$ is the gradient operator.

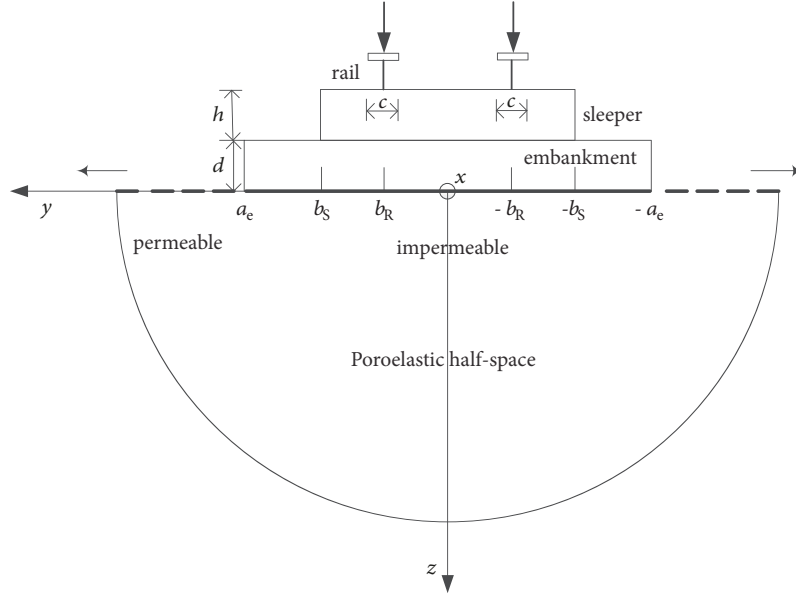


FIGURE 1: The geometry of the semianalytical model.

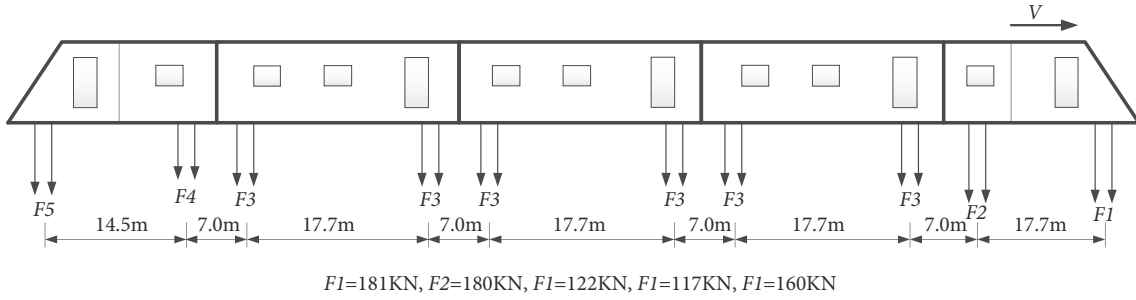


FIGURE 2: The load amplitude and geometric distribution of the high-speed train.

For the saturated poroelastic half-space underneath the embankment, Biot's theory is introduced:

$$\mu \nabla^2 \mathbf{u} + (\lambda + \alpha^2 M + \mu) \nabla (\nabla \cdot \mathbf{u}) + \alpha M \nabla (\nabla \cdot \mathbf{w}) = \rho \ddot{\mathbf{u}} + \rho_f \ddot{\mathbf{w}} \quad (3)$$

$$\alpha M \nabla (\nabla \cdot \mathbf{u}) + M \nabla (\nabla \cdot \mathbf{w}) = \rho_f \ddot{\mathbf{u}} + m_1 \ddot{\mathbf{w}} + b \dot{\mathbf{w}} \quad (4)$$

where the solid displacement vector is defined as $\mathbf{u}(u_x, u_y, u_z)$ and the fluid displacement vector is defined as $\mathbf{w}(w_x, w_y, w_z)$; λ and μ are Lamé constants of the solid skeleton; ρ , ρ_f , and ρ_s are the mass densities of the saturated soil, fluid, and solid skeleton, respectively; $\rho = n\rho_f + (1-n)\rho_s$, in which n is the porosity; $m_1 = \rho_f/n$ is a density-like parameter that depends on ρ_f and the geometry of the pores; α and M are compressibility coefficients of the fluid and solid skeleton; $b = \eta/k$, in which η is the coefficient of fluid viscosity and k is the coefficient of permeability.

The constitutive relations of the soil medium can be expressed as

$$\sigma_{ij} = \lambda \delta_{ij} \theta + \mu (u_{i,j} + u_{j,i}) - \alpha \delta_{ij} p \quad (5)$$

$$p_f = -\alpha M \theta + M \zeta \quad (6)$$

where σ_{ij} is the total stress and p_f is the pore water pressure; $\zeta = -w_{i,i}$; $\theta = u_{i,i}$.

2.2. Boundary Conditions. The boundary conditions applicable to the problem depend on the contact conditions between the embankment and poroelastic half-space, also the conditions between the embankment and the sleeper. Setting the boundary conditions on the sides of embankment layers ($|y| = a_e$) in the following special way is able to facilitate the series expansion of the displacement field in the embankment:

$$\begin{aligned} v_e &= 0 & |y| &= a_e, -d < z < 0 \\ \sigma_{yxe} &= 0 & |y| &= a_e, -d < z < 0 \\ \sigma_{yze} &= 0 & |y| &= a_e, -d < z < 0 \end{aligned} \quad (7)$$

where a_e is half of the embankment width, and d is the embankment thickness. In the above conditions, $\sigma_{yxe} = 0$ and $\sigma_{yze} = 0$ are the natural ones, but $v_e = 0$ is unphysical for

enabling computation. The study by Karlström and Boström [25] showed that the unphysical condition can simulate the vertical displacement of the embankment well when only vertical loads are applied. The above-mentioned conditions can be simplified as

$$\begin{aligned} v_e &= 0 & |y| &= a_e, -d < z < 0 \\ \partial_y u_e &= 0 & |y| &= a_e, -d < z < 0 \\ \partial_y w_e &= 0 & |y| &= a_e, -d < z < 0 \end{aligned} \quad (8)$$

In the present model, two rails are modeled as infinite Euler-Bernoulli beams in the vertical and transverse directions and as the rod equation in the longitudinal direction. A_R is

$$\sigma_{zze} = \begin{cases} J_1 \ddot{w}_e + J_2 \partial_x^4 w_e + J_3 \partial_x^2 \partial_y^2 w_e + J_4 \partial_y^4 w_e, & |y| < b_s, |y| \notin \left[b_R \pm \frac{c}{2} \right] \\ J_1 \ddot{w}_e + I_2 \partial_x^4 w_e + I_3 \partial_x^2 \partial_y^2 w_e + I_4 \partial_y^4 w_e - \frac{F}{c}, & |y| \in \left[b_R \pm \frac{c}{2} \right] \\ 0, & b_s \leq |y| \leq a_e \end{cases} \quad (9)$$

$$\sigma_{yze} = \begin{cases} \frac{(\rho_R A_R \ddot{v}_e + E_R I_{zR} \partial_x^4 v_e)}{c}, & |y| \in \left[b_R \pm \frac{c}{2} \right] \\ 0, & |y| \notin \left[b_R \pm \frac{c}{2} \right] \end{cases} \quad (10)$$

where $I_1 = J_1 + \rho_R A_R / c$, $J_1 = \rho_s h$, $I_2 = J_2 + E_R I_{yR} / c$, $J_2 = (h^3 / 12)(E_{Sx}^2 / (E_{Sx} - E_{Sk} v_{Sxk}^2))$, $I_3 = J_3$, $J_3 = (h^3 / 6)(E_{Sk} E_{Sx} v_{Sxk} / (E_{Sx} - E_{Sk} v_{Sxk}^2) + 2G_{Sx})$, $I_4 = J_4$, $J_4 = (h^3 / 12)(E_{Sk} E_{Sx} / (E_{Sx} - E_{Sk} v_{Sxk}^2))$.

The longitudinal shear stress σ_{xze} can be given by the rod equation of the rails:

$$\sigma_{xze} = \begin{cases} \frac{(\rho_R A_R \ddot{u}_e - E_R A_R \partial_x^2 u_e)}{c}, & |y| \in \left[b_R \pm \frac{c}{2} \right] \\ 0, & |y| \notin \left[b_R \pm \frac{c}{2} \right] \end{cases} \quad (11)$$

The ground is assumed to be bonded with the embankment perfectly; hence the displacement and stress compatibility conditions can be expressed as

$$\mathbf{u} = \mathbf{u}_e, \quad |y| < a_e, \quad z = 0 \quad (12)$$

$$\boldsymbol{\sigma} = \begin{cases} \boldsymbol{\sigma}_e, & |y| < a_e, \quad z = 0 \\ 0 & |y| > a_e, \quad z = 0 \end{cases} \quad (13)$$

where the displacement vector of the saturated half-space is defined as $\mathbf{u}(u_x, u_y, u_z)$ and the stress vector is defined as $\boldsymbol{\sigma}(\sigma_z, \sigma_{zx}, \sigma_{zy})$.

For the case of permeable boundary at the ground surface, all stresses from the embankment are transmitted to the solid skeleton of poroelastic ground. Thus the pore pressure is zero at the interface. In contrast, for the case of impermeable boundary condition, stresses from the embankment are

transmitted to both the fluid and soil skeleton of poroelastic ground, which implies that the pore water pressure is nonzero. The hydraulic boundary condition can be expressed as follows.

For the permeable boundary condition ($z=0$):

$$p_f = 0 \quad (14)$$

For the impermeable boundary condition ($z=0$):

$$\frac{dp_f}{dz} = 0 \quad (15)$$

2.3. Analytical Solution. In order to solve Lamé equations of the embankment layer, three potentials for longitudinal (P), horizontal transverse (SH), and vertical transverse (SV) waves, which are denoted by φ , ψ_{SH} , and ψ_{SV} , respectively, are employed to decompose the displacement field (for the detailed solution procedure, see Cao et al. [28]):

$$\mathbf{u}_e = \nabla \varphi + \nabla \times (\mathbf{e}_z \psi_{SH}) + \nabla \times \nabla \times (\mathbf{e}_z \psi_{SV}) \quad (16)$$

The Fourier transform pair with respect to t is defined as

$$\tilde{f}(\omega) = \int_{-\infty}^{+\infty} f(t) e^{i\omega t} dt \quad (17)$$

$$f(t) = \frac{1}{2\pi} \int_{-\infty}^{+\infty} \tilde{f}(\omega) e^{-i\omega t} d\omega \quad (18)$$

The Fourier transform pair with respect to x is defined as

$$\bar{g}(q) = \int_{-\infty}^{+\infty} g(x) e^{-iqx} dx \quad (19)$$

$$g(x) = \frac{1}{2\pi} \int_{-\infty}^{+\infty} \bar{g}(q) e^{iqx} dq \quad (20)$$

Meanwhile to meet the special boundary conditions of the sides of embankment in the y direction, Fourier series expansions with respect to the three potentials mentioned above are introduced:

$$\hat{\varphi} = \sum_{m=0}^{\infty} (D_{1m} \sin h_{pm}z + E_{1m} \cos h_{pm}z) \cos p_m y \quad (21)$$

$$\hat{\psi}_{SH} = \sum_{m=1}^{\infty} (D_{2m} \sin h_{sm}z + E_{2m} \cos h_{sm}z) \sin p_m y \quad (22)$$

$$\hat{\psi}_{SV} = \sum_{m=0}^{\infty} (E_{3m} \sin h_{sm}z - D_{3m} \cos h_{sm}z) \cos p_m y \quad (23)$$

where $p_m = m\pi/a_e$ is wavenumber in the y direction; D_{nm} and E_{nm} are unknown constants ($n=1, 2, 3$); $k_p = \omega/c_p$ and $k_s = \omega/c_s$, in which c_p denotes the compression wave speed of the embankment and is calculated as $c_p = ((\lambda_e + 2\mu_e)/\rho_e)^{1/2}$, and c_s is the shear wave speed defined as $c_s = (\mu_e/\rho_e)^{1/2}$; $h_{pm} = (k_p^2 - q^2 - p_m^2)^{1/2}$, $h_{sm} = (k_s^2 - q^2 - p_m^2)^{1/2}$ with $\text{Im } h_{pm} \geq 0$ and $\text{Im } h_{sm} \geq 0$.

Adopting (21)-(23) together with (16), the embankment displacements are expressed as

$$\hat{u}_e = \sum_{m=0}^{\infty} \hat{u}_m(z) \cos p_m y \quad (24)$$

$$\hat{v}_e = \sum_{m=1}^{\infty} \hat{v}_m(z) \sin p_m y \quad (25)$$

$$\hat{w}_e = \sum_{m=0}^{\infty} \hat{w}_m(z) \cos p_m y \quad (26)$$

where

$$\hat{u}_m(z) = \sum_{n=1}^3 \alpha_{nm} (D_{nm} \sin k_{nm}z + E_{nm} \cos k_{nm}z) \quad (27)$$

$$\hat{v}_m(z) = \sum_{n=1}^3 \beta_{nm} (D_{nm} \sin k_{nm}z + E_{nm} \cos k_{nm}z) \quad (28)$$

$$\hat{w}_m(z) = \sum_{n=1}^3 \gamma_{nm} (D_{nm} \cos k_{nm}z - E_{nm} \sin k_{nm}z) \quad (29)$$

The definition for the parameters α_{nm} , β_{nm} , γ_{nm} , and k_{nm} is listed in Table 1.

Substituting (24)-(26) into (2), the stresses in the embankment can be derived as follows:

$$\hat{\sigma}_{xze} = \sum_{m=0}^{\infty} \hat{\sigma}_{xzm}(z) \cos p_m y \quad (30)$$

TABLE 1: Displacement coefficients.

n	1	2	3
α_{nm}	iq	p_m	iqh_{sm}
β_{nm}	$-p_m$	$-iq$	$-p_m h_{sm}$
γ_{nm}	h_{pm}	0	$-(p_m^2 + q^2)$
k_{nm}	h_{pm}	h_{sm}	h_{sm}

$$\hat{\sigma}_{yze} = \sum_{m=0}^{\infty} \hat{\sigma}_{yzm}(z) \sin p_m y \quad (31)$$

$$\hat{\sigma}_{zze} = \sum_{m=0}^{\infty} \hat{\sigma}_{zzm}(z) \cos p_m y \quad (32)$$

where

$$\hat{\sigma}_{xzm}(z) = \sum_{n=1}^3 \mu_e \xi_{nm} (D_{nm} \cos k_{nm}z - E_{nm} \sin k_{nm}z) \quad (33)$$

$$\hat{\sigma}_{yzm}(z) = \sum_{n=1}^3 \mu_e \zeta_{nm} (D_{nm} \cos k_{nm}z - E_{nm} \sin k_{nm}z) \quad (34)$$

$$\hat{\sigma}_{zzm}(z) = \sum_{n=1}^3 \mu_e \eta_{nm} (D_{nm} \sin k_{nm}z + E_{nm} \cos k_{nm}z) \quad (35)$$

ξ_{nm}^j , ζ_{nm}^j , and η_{nm}^j are given as follows:

$$\xi_{nm} = k_{nm} \alpha_{nm} + iq \gamma_{nm} \quad (36)$$

$$\zeta_{nm} = k_{nm} \beta_{nm} - p_m \gamma_{nm} \quad (37)$$

$$\eta_{nm} = \left(\left(\frac{k_s}{k_p} \right)^2 - 2 \right) (iq \alpha_{nm} + p_m \beta_{nm}) - \left(\frac{k_s}{k_p} \right)^2 k_{nm} \gamma_{nm} \quad (38)$$

Analytical solutions to the dynamic equations of motion for a fully saturated poroelastic medium (see (3)-(4)) can be obtained by applying a triple Fourier transform.

The Fourier transform pair with respect to y is defined as

$$\bar{g}(p) = \int_{-\infty}^{+\infty} g(y) e^{-ipy} dy \quad (39)$$

$$g(y) = \frac{1}{2\pi} \int_{-\infty}^{+\infty} \bar{g}(p) e^{ipy} dp \quad (40)$$

The dynamic equations of saturated soil can be solved in the transformed domain and the solutions are expressed as

$$\bar{p}_f = A e^{-\gamma_1 z} + B e^{-\gamma_2 z} \quad (41)$$

$$\bar{u}_x = -\frac{i}{q} \left\{ [\chi_1 + a_1 (q^2 - L_1^2)] A e^{-\gamma_1 z} \right. \quad (42)$$

$$\left. + [\chi_2 + a_2 (q^2 - L_2^2)] B e^{-\gamma_2 z} + (C\gamma_3 + Dp) e^{-\gamma_3 z} \right\}$$

$$\bar{u}_y = -ip (a_1 A e^{-\gamma_1 z} + a_2 B e^{-\gamma_2 z}) + i D e^{-\gamma_3 z} \quad (43)$$

$$\bar{u}_z = \gamma_1 a_1 A e^{-\gamma_1 z} + \gamma_2 a_2 B e^{-\gamma_2 z} + C e^{-\gamma_3 z} \quad (44)$$

Substituting (42)-(44) into (5), the stresses in the poroelastic half-space are given as

$$\begin{aligned} \bar{\sigma}_{xz} = & \frac{\mu i}{q} [\gamma_1 g_1 A e^{-\gamma_1 z} + \gamma_2 g_2 B e^{-\gamma_2 z} \\ & + (C\gamma_3^2 + Cq^2 + D\gamma_3 p) e^{-\gamma_3 z}] \end{aligned} \quad (45)$$

$$\begin{aligned} \bar{\sigma}_{yz} = & \mu i [2p\gamma_1 a_1 A e^{-\gamma_1 z} + 2p\gamma_2 a_2 B e^{-\gamma_2 z} \\ & + (Cp - D\gamma_3) e^{-\gamma_3 z}] \end{aligned} \quad (46)$$

$$\bar{\sigma}_{zz} = g_3 A e^{-\gamma_1 z} + g_4 B e^{-\gamma_2 z} - 2\mu\gamma_3 C e^{-\gamma_3 z} \quad (47)$$

where A , B , C , and D are the unknown constants. Other coefficients are given in the Appendix.

At the surface of the half-space ($z=0$), the following equations are obtained by applying Fourier transform with respect to y to the stress compatibility condition:

$$\begin{aligned} \frac{\mu i}{q} \{ \gamma_1 g_1 A + \gamma_2 g_2 B + [C(\gamma_3^2 + q^2) + D\gamma_3 p] \} \\ = \sum_{m=0}^{\infty} \bar{\sigma}_{xzm}(0) f_m(p) \end{aligned} \quad (48)$$

$$\begin{aligned} \mu i [2p\gamma_1 a_1 A e^{-\gamma_1 z} + 2p\gamma_2 a_2 B e^{-\gamma_2 z} + (Cp - D\gamma_3) e^{-\gamma_3 z}] \\ = \sum_{m=1}^{\infty} \bar{\sigma}_{yzm}(0) g_m(p) \end{aligned} \quad (49)$$

$$g_3 A e^{-\gamma_1 z} + g_4 B e^{-\gamma_2 z} - 2\mu\gamma_3 C e^{-\gamma_3 z} = \sum_{m=0}^{\infty} \bar{\sigma}_{zzm}(0) f_m(p) \quad (50)$$

where $f_m(p)$ and $g_m(p)$ are defined as

$$f_m(p) = \int_{-a_e}^{a_e} \cos(p_m y) e^{-ipy} dy \quad (51)$$

$$g_m(p) = \int_{-a_e}^{a_e} \sin(p_m y) e^{-ipy} dy \quad (52)$$

At the interface between the embankment and the poroelastic half-space ($z=0$), the drainage conditions are assumed to be fully permeable or fully impermeable. The additional hydraulic boundary condition should be added.

For the permeable boundary condition ($z=0$):

$$p_f = A + B = 0 \quad (53)$$

For the impermeable boundary condition ($z=0$):

$$\frac{dp_f}{dz} = -\gamma_1 A - \gamma_2 B = 0 \quad (54)$$

By applying (48)-(50) and (53)-(54), the unknown coefficients A , B , C , and D can be expressed by D_{nm}^j and E_{nm}^j .

The application of the displacement continuity condition between the embankment and the poroelastic half-space over the width of the embankment gives the remaining unknowns D_{nm}^j and E_{nm}^j . According to the orthogonality of

trigonometric series, each mode m of the series gives an independent equation, denoted as m' :

$$\begin{aligned} \frac{1}{2\pi} \int_{-\infty}^{+\infty} -\frac{i}{q} \{ [\chi_1 + a_1(q^2 - L_1^2)] A \\ + [\chi_2 + a_2(q^2 - L_2^2)] B + (C\gamma_3 + Dp) \} f_{m'}(p) dp \end{aligned} \quad (55)$$

$$= \frac{2a_e}{\varepsilon_{m'}} \hat{u}_{m'}(0)$$

$$\begin{aligned} \frac{1}{2\pi} \int_{-\infty}^{+\infty} [-ip(a_1 A + a_2 B) + iD] g_{m'}(p) dp \\ = -a_e \hat{v}_{m'}(0) \end{aligned} \quad (56)$$

$$\frac{1}{2\pi} \int_{-\infty}^{+\infty} (\gamma_1 a_1 A + \gamma_2 a_2 B + C) f_{m'}(p) dp = \frac{2a_e}{\varepsilon_{m'}} \hat{w}_{m'}(0) \quad (57)$$

where $\varepsilon_{m'}$ is the Neumann factor, defined as $\varepsilon_0 = 1$ for $m' = 0$ and $\varepsilon_{m'} = 2$ for $m' \geq 1$.

For the stress conditions at the top surface of the embankment (see (8)-(10)), a similar inverse Fourier series with respect to y over the width $2a_e$ is employed to obtain the following equations:

$$\begin{aligned} \bar{\sigma}_{zzm'}(-d) \frac{2a_e}{\varepsilon_{m'}} = \sum_{m=0}^{\infty} (K_{zR} \Gamma_{m,m'} + K_{zS} \Delta_{m,m'}) \hat{w}_m(-d) \\ - \frac{\hat{F}}{c} \Gamma_{0,m'} \end{aligned} \quad (58)$$

$$\bar{\sigma}_{yzm'}(-d) a_e = \sum_{m=1}^{\infty} K_{yR} \hat{v}_m(-d) \Omega_{m,m'} \quad (59)$$

$$\bar{\sigma}_{xzm'}(-d) \frac{2a_e}{\varepsilon_{m'}} = \sum_{m=0}^{\infty} K_{xR} \hat{u}_m(-d) \Gamma_{m,m'} \quad (60)$$

where

$$\begin{aligned} K_{zR} = & -\frac{A_R \rho_R}{c} \omega^2 + \frac{E_R I_{yR}}{c} q^4, \\ K_{zS} = & -J_1 \omega^2 + J_2 q^4 + J_3 q^2 p_m^2 + J_4 p_m^4, \\ K_{yR} = & -\frac{A_R \rho_R}{c} \omega^2 + \frac{E_R I_{zR}}{c} q^4, \\ K_{xR} = & -\frac{A_R \rho_R}{c} \omega^2 + \frac{E_R A_R}{c} q^2. \end{aligned} \quad (61)$$

$\Gamma_{m,m'}$, $\Omega_{m,m'}$, and $\Delta_{m,m'}$ can be calculated by the following integral formulas:

$$\begin{aligned} \Gamma_{m,m'} = & \int_{-b_R - c/2}^{-b_R + c/2} \cos p_m y \cos p_{m'} y dy \\ & + \int_{b_R - c/2}^{b_R + c/2} \cos p_m y \cos p_{m'} y dy \end{aligned} \quad (62)$$

TABLE 2: Parameters for the railway track.

Parameter	Value
Sectional area for the rail, A_R (cm ²)	76.87
Modulus of elasticity for the rail, E_R (GPa)	210
Density for the rail, ρ_R (kg/m ³)	7850
Area moment of inertia about the y axis for the rail, I_{yR} (cm ⁴)	3055
Area moment of inertia about the z axis for the rail, I_{zR} (cm ⁴)	516.4
Half distance between the rails, b_R (m)	0.75
Modulus of elasticity in the k direction for the sleeper, E_{Sk} (MPa)	38450
Modulus of elasticity in the x direction for the sleeper, E_{Sx} (MPa)	0
Sleeper density, ρ_s (kg/m ³)	635
Half width of the sleeper, b_s (m)	1.26
Height of the sleeper, h (m)	0.233

TABLE 3: Parameters for the embankment.

Parameter	Value
Lamé constants of the embankment, μ_e (MPa)	5.4
Poisson's ratio, ν_e	0.3
Density of the embankment, ρ_e (kg/m ³)	1800
Coefficient of material damping, δ_e	0.03
Height of the embankment, d (m)	0.5
Width of the embankment, a_e (m)	4

$$\Omega_{m,m'} = \int_{-b_R-c/2}^{-b_R+c/2} \sin p_m y \sin p_{m'} y dy + \int_{b_R-c/2}^{b_R+c/2} \sin p_m y \sin p_{m'} y dy \quad (63)$$

$$\Delta_{m,m'} = \int_{-b_s}^{-b_s} \cos p_m y \cos p_{m'} y dy \quad (64)$$

where \hat{F} is the train axle load in the transformed domain. For the train load with a constant speed, it can be expressed as

$$\hat{F} = F_0 \int_{-\infty}^{\infty} \int_{-\infty}^{\infty} \delta(x - V_0 t) e^{i(\omega t - qx)} dx dt = 2\pi F_0 \delta(\omega + qV - \Omega) \quad (65)$$

where V is the train speed, F_0 is the load amplitude, and Ω is the excitation frequency of the train load.

3. Numerical Results and Analysis

Referring to the work by Cao et al. [28], the parameters for the railway track and the embankment are listed in Tables 2 and 3. The parameters describing the properties of the saturated poroelastic half-space are listed in Table 4. The parameters will be selected from Tables 2–4 unless otherwise specified. The effects of the hydraulic boundary condition between the embankment and saturated poroelastic half-space on the dynamic response of the embankment-ground system are investigated for two moving train speeds ($V=70$ km/h and $V=250$ km/h) below and above the critical speed, respectively.

TABLE 4: Parameters for the saturated poroelastic half-space.

Parameter	Value
Lamé constants of the half-space, μ (MPa)	6.0
Soil density, ρ_s (kg/m ³)	1816
Water density, ρ_f (kg/m ³)	1000
Porosity, n	0.4
A density-like parameter, m_1 (kg/m ³)	2500
Coefficient of material damping, δ	0.05
Permeability, b (N s/m ⁴)	10^6
Compressibility of the soil particle, α	0.97
Poisson's ratio, ν	0.35
Compressibility of the fluid, M (MPa)	5000

3.1. Comparison with Existing Works. In order to verify the present work, results calculated by the present model are compared with those obtained by Karlström and Boström [25], in which the single-phase elastic material was used to model the half-space instead of using a two-phase saturated soil model. A viscoelastic half-space can be modeled by choosing negligibly small values of the poroelastic parameters (ρ_f , b , M , and α are set to be 10^{-4}). The vertical displacements at the central line of the top surface of embankment due to a moving train with speed of 70 km/h are presented in Figure 3(a). It can be seen that the two results are in good consistency. To further verify the correctness of the proposed analytical solution, the numerical results obtained by the present model are compared with the field measurements carried out by Madshus and Kaynia [26]. In the field test, the ground-borne vibrations generated by X2000 trains running on a soft soil site at Lesgard in Sweden were monitored. In order to make the calculations obtained by the proposed method comparable with the field measurements, the soil and track parameters are selected as those used in the work by Madshus and Kaynia [26]. The measurement position is chosen at the central line of the top surface of embankment, and the train velocity is 185 km/h. As seen in Figure 3(b), in a general trend the results predicted by the proposed analytical model agree well with those measured in the field test.

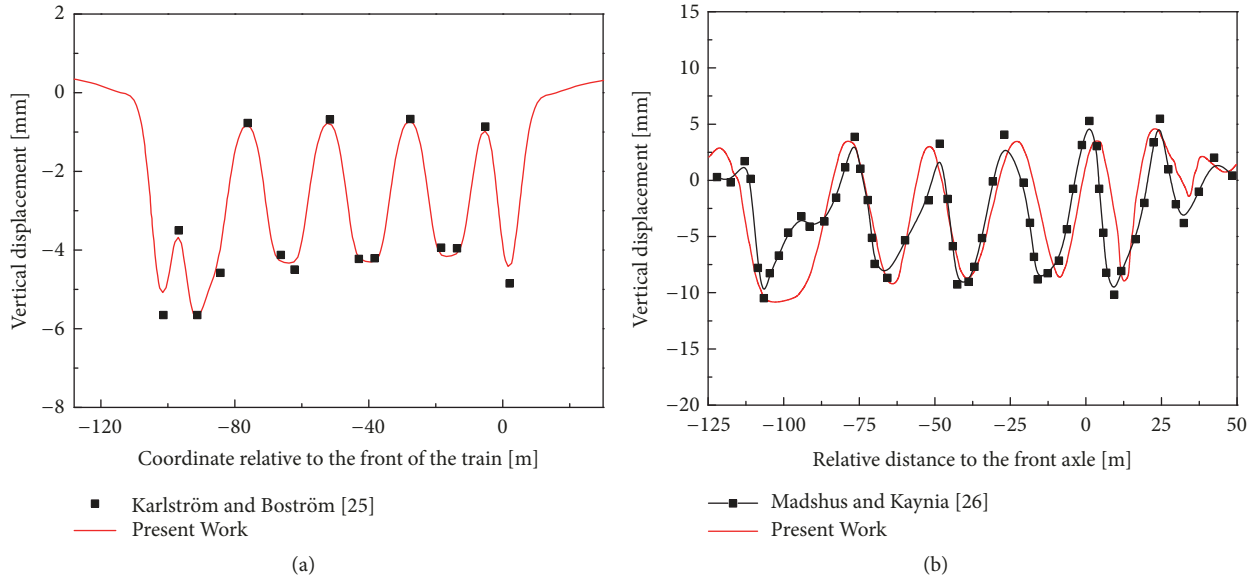


FIGURE 3: Comparisons of present results with (a) the results of [25] and (b) field measurements [26].

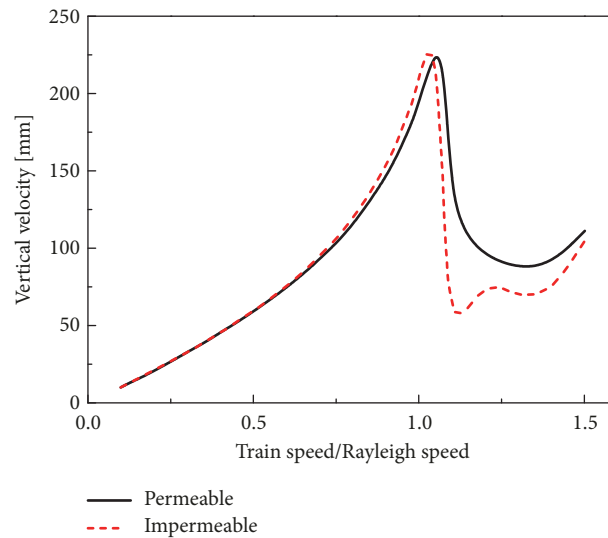


FIGURE 4: The maximum vertical velocity at the ground surface versus the train speed V .

3.2. Dynamic Response of the Ground Generated by Moving Constant Loads. In Figure 4, the maximum vertical velocity at the ground surface ($y=0\text{m}$, $z=0\text{m}$) versus the train speed V is presented. Two hydraulic boundary cases, i.e., the permeable and impermeable ground surface, are considered. It is shown that the maximum vertical velocity at the ground surface varies with the train speed and reaches a sharp peak at a certain velocity, which is defined as the critical velocity of the embankment-ground system. The critical velocity is near $1.05 V_s$ (V_s is the shear wave velocity of the ground); the reason why the critical velocity is higher than the shear wave velocity of the ground is that the embankment is more rigid than the saturated ground. No obvious difference in the vertical velocity for the permeable and impermeable boundary cases is observed at the low train speed range.

However, when the train speed approaches the critical speed, the vertical velocity for the two cases becomes quite different.

In Figure 5, the time history of the train-induced vertical velocity at the ground surface ($x=0$, $y=0$, $z=0$) is presented at a train speed of 250 km/h. From Figure 5(a), it can be clearly observed that the vertical velocity reaches a positive peak value at the position of wheel pairs but a negative peak after the wheel pairs have passed by. The largest vertical velocity is 135 mm/s for the permeable hydraulic boundary and twice more than that for the impermeable hydraulic boundary. The frequency spectrum in Figure 5(b) presents a wave-like pattern with peaks which correspond to the geometric distribution of train axle loads under certain train speed. A significant distinction of the vertical velocity can be observed between the two cases, especially at the peaks. The

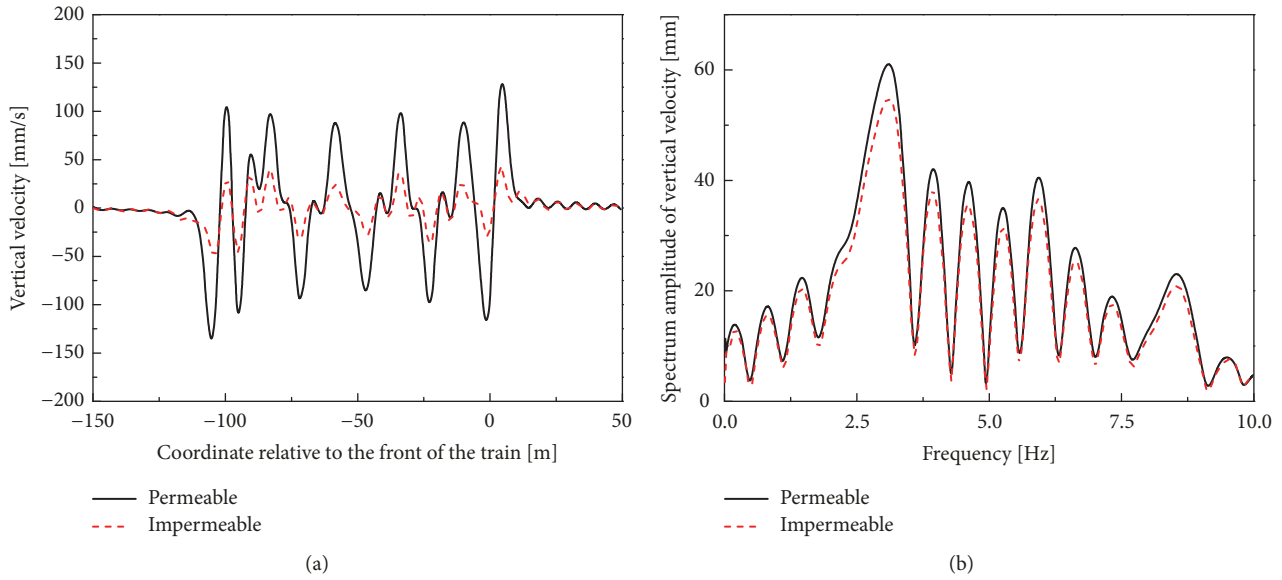


FIGURE 5: The vertical velocity at the train speed of 250 km/h: (a) in the time domain and (b) in the frequency domain.

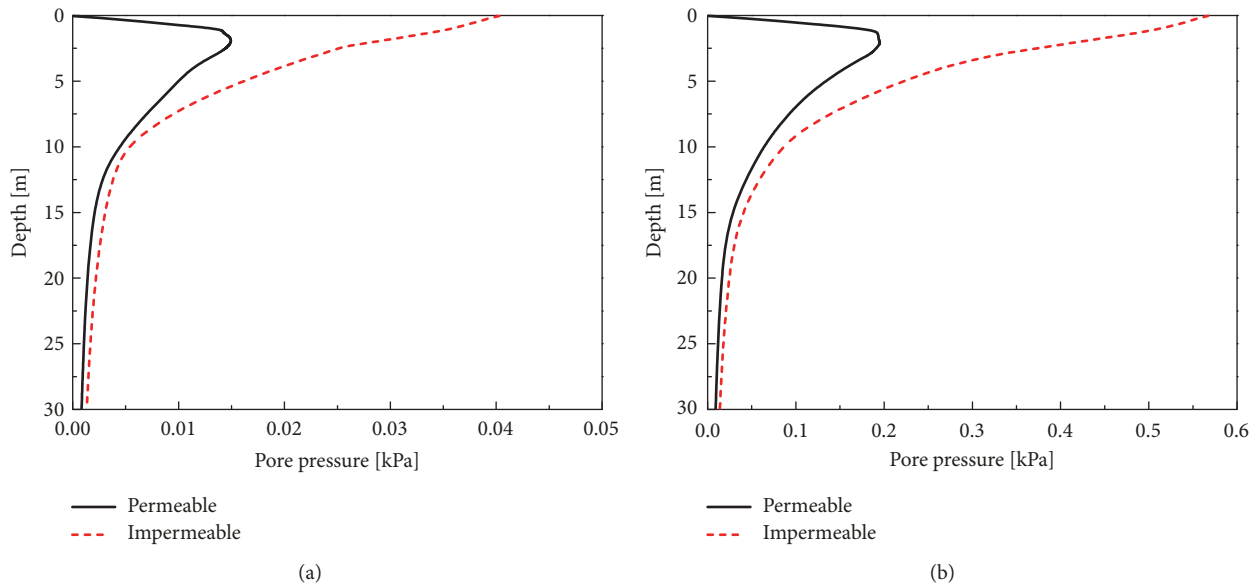


FIGURE 6: The maximum pore pressure versus depth in a high-permeability saturated soil ($b=1.0 \times 10^6 \text{ N}\cdot\text{s}/\text{m}^4$): (a) $V=70 \text{ km/h}$ and (b) $V=250 \text{ km/h}$.

results of Figures 4 and 5 can be explained as follows: for the high train speed, the frequency content spreads in the high frequency range, which implies that obvious relative motion between the solid skeleton and fluid occurs, and as a result the hydraulic boundary of the ground surface has a significant effect on the velocity response.

The maximum pore pressure versus depth under a constant moving load for $V=70 \text{ km/h}$ and $V=250 \text{ km/h}$ is shown in Figure 6. The effect of the hydraulic boundary condition on the pore water pressure is analyzed. The value of b , a parameter reflecting the permeability of the soil, is chosen to be $1.0 \times 10^6 \text{ N}\cdot\text{s}/\text{m}^4$. It should be pointed out that b is inversely

proportional to the soil permeability. As shown in Figure 6, for the permeable case the maximum pore pressure increases with depth and reaches a peak value at $z=2.5 \text{ m}$ and then rapidly decreases to a constant value. For the impermeable case the maximum pore pressure decreases monotonously, and with the depths larger than $z=20 \text{ m}$, the pore pressure response becomes very small. The comparison of Figures 6(a) and 6(b) shows that the maximum pore pressure increases with the train speed over the depth considered. For example, when the train speed increases from 70 km/h to 250 km/h , the peak pore pressure increases from 0.015 kPa to 0.22 kPa for the permeable case and from 0.04 kPa to 0.62 kPa for the

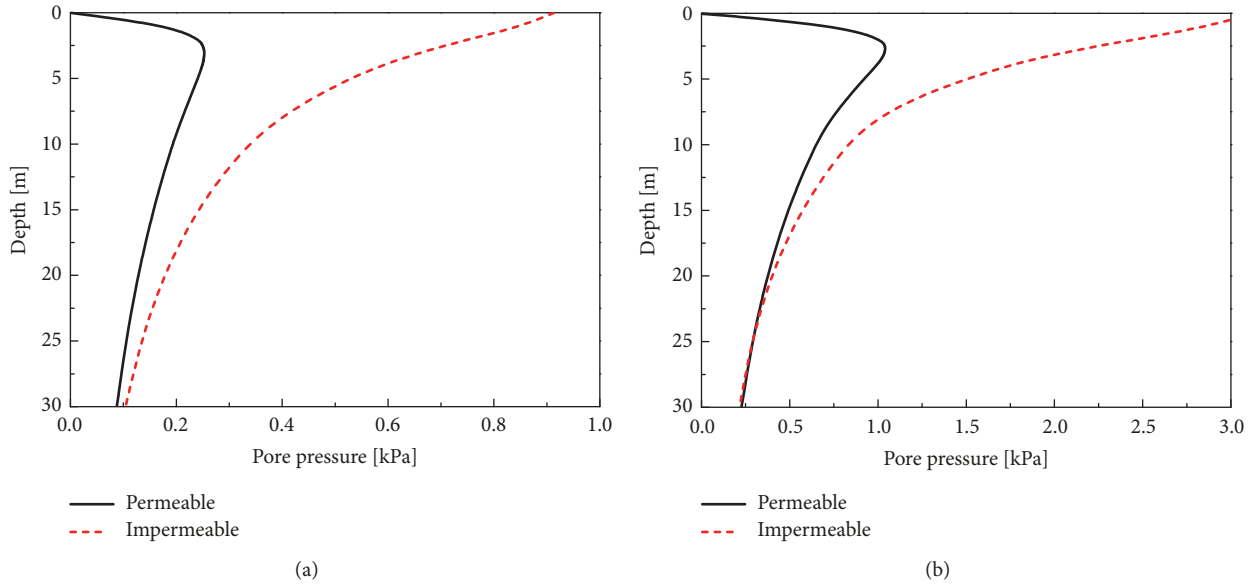


FIGURE 7: The maximum pore pressure versus depth in a low-permeability saturated soil ($b = 1.0 \times 10^9 \text{ N}\cdot\text{s}/\text{m}^4$): (a) $V=70 \text{ km/h}$ and (b) $V=250 \text{ km/h}$.

impermeable case. The ground with impermeable surface has a much larger pore water pressure than that with permeable surface. Furthermore, it can be seen that the pore pressure difference under two drainage conditions is mainly distributed in the region near the ground surface and decreases for deeper depths.

Figure 7 shows the maximum pore pressure against depth under a moving train for a low-permeability soil ($b=1.0 \times 10^9 \text{ N}\cdot\text{s}/\text{m}^4$). By comparing Figure 6 with Figure 7, it can be found that the train-induced pore pressure in the low-permeability soil is much larger than the pore pressure in the high-permeability soil.

3.3. Dynamic Response of the Ground Generated by Moving Harmonic Loads. In reality, the contact surface between the wheels and rails is usually uneven, and hence the harmonic loads with self-frequency are suitable for modeling the dynamic loads between the track and the rail [10]. In order to investigate the ground vibrations generated by the dynamic wheel-rail interaction, the moving harmonic loads are used to simulate the train loads in this section.

The vertical velocity on ground surface generated by a moving train with self-excitation frequency of 10 Hz is presented in Figures 8 and 9 for the train speeds 70 km/h and 250 km/h, respectively. For both train speeds, the vertical velocity for the permeable case is similar to the values for the impermeable case. Thus, the effect of the hydraulic boundary condition of the ground surface on the velocity response is quite limited for moving trains with a low self-excitation frequency of 10 Hz.

The maximum pore pressure in the poroelastic ground with low and high soil permeability coefficients generated by a moving train with self-excitation frequency $f_0=10 \text{ Hz}$ is presented in Figures 10 and 11. In Figure 10(a), for the case of $b=1.0 \times 10^6 \text{ N}\cdot\text{s}/\text{m}^4$ it can be seen that the maximum pore

pressure for the impermeable case is larger than that for the permeable case near the ground surface. The values of pore pressure for two cases equal to each other at $z=2.5 \text{ m}$, and for deeper depths the maximum pore pressure for the permeable case exceeds the pore pressure for the impermeable case. A similar trend can be observed in Figure 10(b). The train-induced pore pressure in a low-permeability soil ($b=1.0 \times 10^9 \text{ N}\cdot\text{s}/\text{m}^4$) is presented in Figure 11. It is observed that the pore pressure response mainly occurs in the depths shallower than $z=10 \text{ m}$, and the effect of the hydraulic boundary condition on the pore pressure is obvious only near the ground surface.

The vertical velocity on ground surface induced by a moving train with self-excitation frequency of 30 Hz for two train speeds is presented in Figures 12 and 13. At the train speed $V=70 \text{ km/h}$, as shown in Figure 12, the vertical velocity for the impermeable case is about 25% larger than that for the permeable case. The vertical velocity is mainly distributed in the frequency range of 20-40 Hz, and most of the frequency components for the impermeable case are larger than those for the permeable case, especially at the peak values. In Figure 13(a), for the train speed of 250 km/h, a huge discrepancy of the vertical velocity between the two cases can be observed, and the waves propagate over a wider area and attenuate more slowly. Figures 12 and 13 show that the frequency components are mainly distributed around 30 Hz, and this is due to the well-known Doppler effects. The frequency range can be calculated by $f_{cr} = f_0/2\pi(1 \pm V/c_R)$ where f_{cr} is the upper and lower limit of the frequency range.

The maximum pore pressure plotted against the depth to a moving train with self-excitation frequency of 30 Hz is shown in Figure 14 for a high soil permeability ($b=1.0 \times 10^6 \text{ N}\cdot\text{s}/\text{m}^4$). In a general trend the pore pressure for the two cases decreases with depth and the fluctuation pattern is due to the wave propagations in the ground. When $V=70 \text{ km/h}$, the

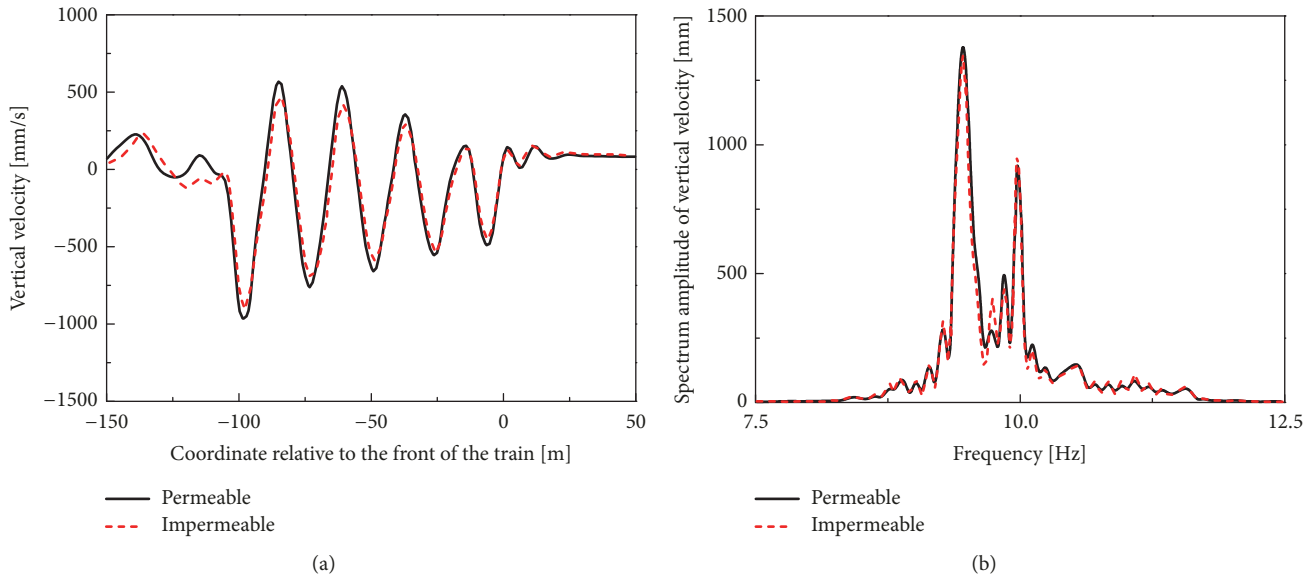


FIGURE 8: The vertical velocity under a moving train at $V=70$ km/h with $f_0 = 10$ Hz: (a) in the time domain and (b) in the frequency domain.

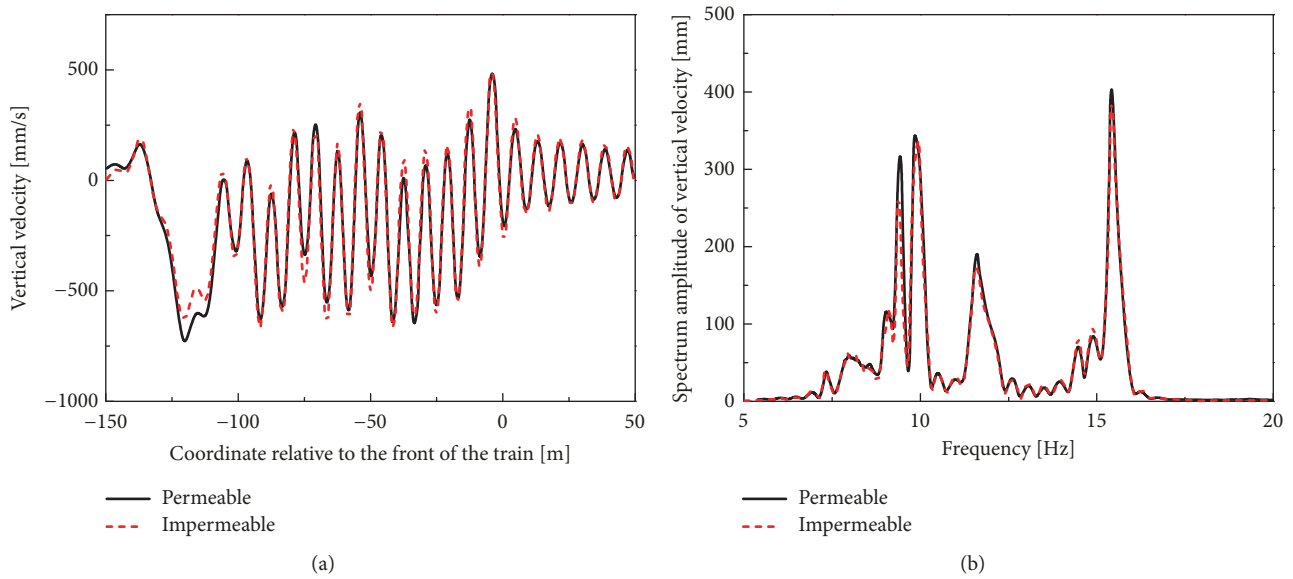


FIGURE 9: The vertical velocity under a moving train at $V=250$ km/h with $f_0=10$ Hz: (a) in the time domain and (b) in the frequency domain.

local maximum value of the pore pressure for the permeable case is 100% larger than that for the impermeable case. When $V=250$ km/h, the difference of the local maximum value between the two hydraulic boundary conditions is 50%. The difference of the pore water pressure between the two cases disappears gradually as the depth increases. Figure 15 shows the pore pressure in the saturated ground with $b=1.0 \times 10^9$ N·s/m⁴. It is observed that the magnitude of the pore pressure for the two cases is similar. This is due to the fact that the interface between the embankment and the half-space presents an impermeable behavior in low-permeability soil even assuming the hydraulic boundary condition to be permeable. As shown in Figure 15(b), the phase difference

of the pore pressure is obvious at the high train speed of 250 km/h.

3.4. Influence of the Load Excitation Frequency on the Velocity Response. In order to investigate the effect of load excitation frequency on the velocity response specifically, the velocity response at the ground surface is plotted against the load self-excitation frequency in Figures 16 and 17. In a general trend the vertical velocity to a moving train firstly increases with the increase of self-excitation frequency and reaches its maximum value at a load frequency around 10 Hz and then decreases as the frequency increases further. The effect of the hydraulic boundary at the ground surface on the

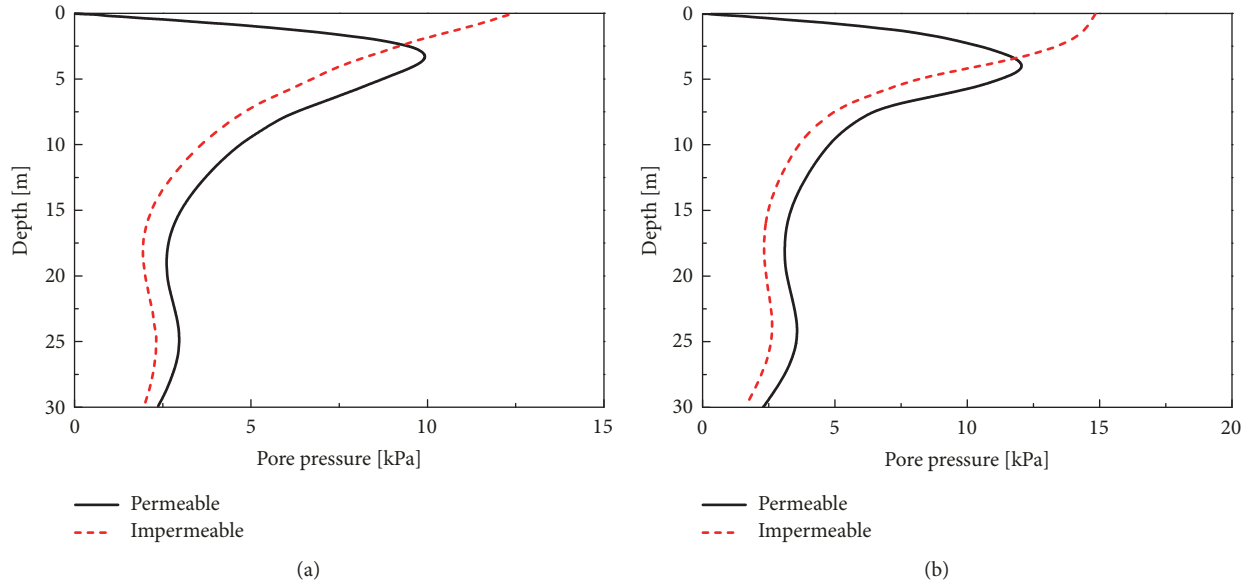


FIGURE 10: The maximum pore pressure under a moving train with $f_0 = 10$ Hz ($b = 1.0 \times 10^6$ N·s/m⁴): (a) $V = 70$ km/h and (b) $V = 250$ km/h.

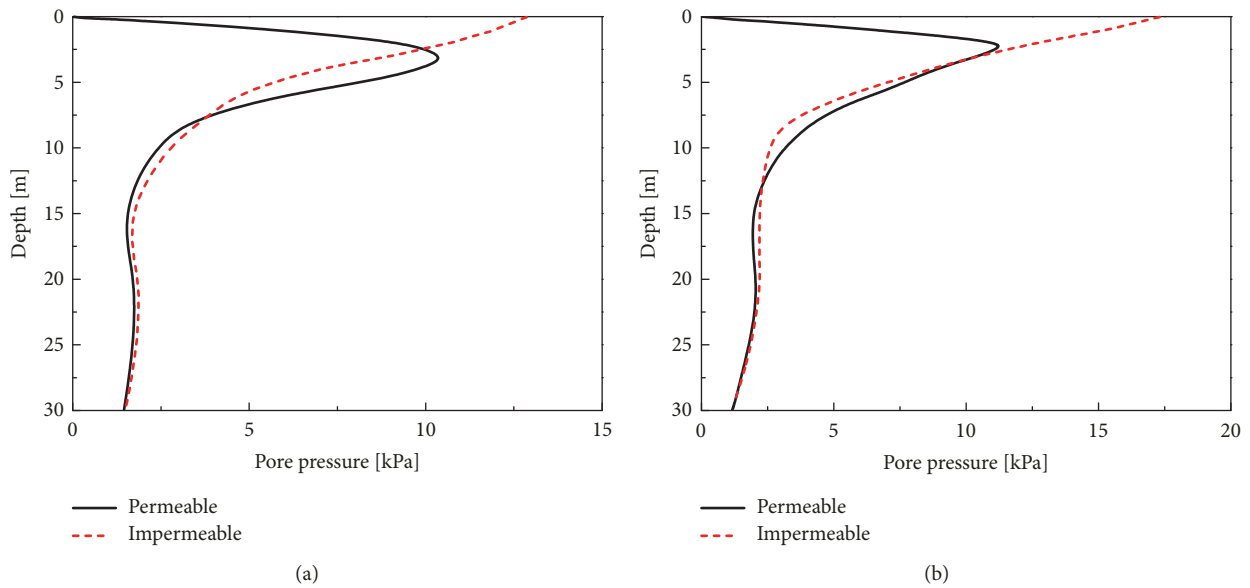


FIGURE 11: The maximum pore pressure under a moving train with $f_0 = 10$ Hz at ($b = 1.0 \times 10^9$ N·s/m⁴): (a) $V = 70$ km/h and (b) $V = 250$ km/h.

vertical velocity response becomes more significant at higher frequencies. The comparison between Figures 16 and 17 shows that the effect of the hydraulic boundary on the velocity response is reduced with the increase of b (a decrease of the soil permeability) due to the fact that relative motion between the soil skeleton and the fluid is restrained in the low-permeability ground.

4. Conclusions

In this work, a three-dimensional model is proposed to investigate the influence of hydraulic boundary condition

between the embankment and poroelastic half-space on the free-field response induced by moving trains. The train-induced vibration prediction model consists of a detailed railway track and a saturated ground. The saturated ground is governed by Biot's theory, and the linearized dynamic equations of motion for fully saturated poroelastic half-space and the embankment are solved by applying Fourier transform and Fourier series. Dynamic response of the ground with a permeable and impermeable surface induced by a moving train load is investigated and the effect of the hydraulic boundary condition on the vertical velocity and pore pressure in the ground is analyzed. In addition, a parametric analysis is performed for different train speeds, load frequencies, and

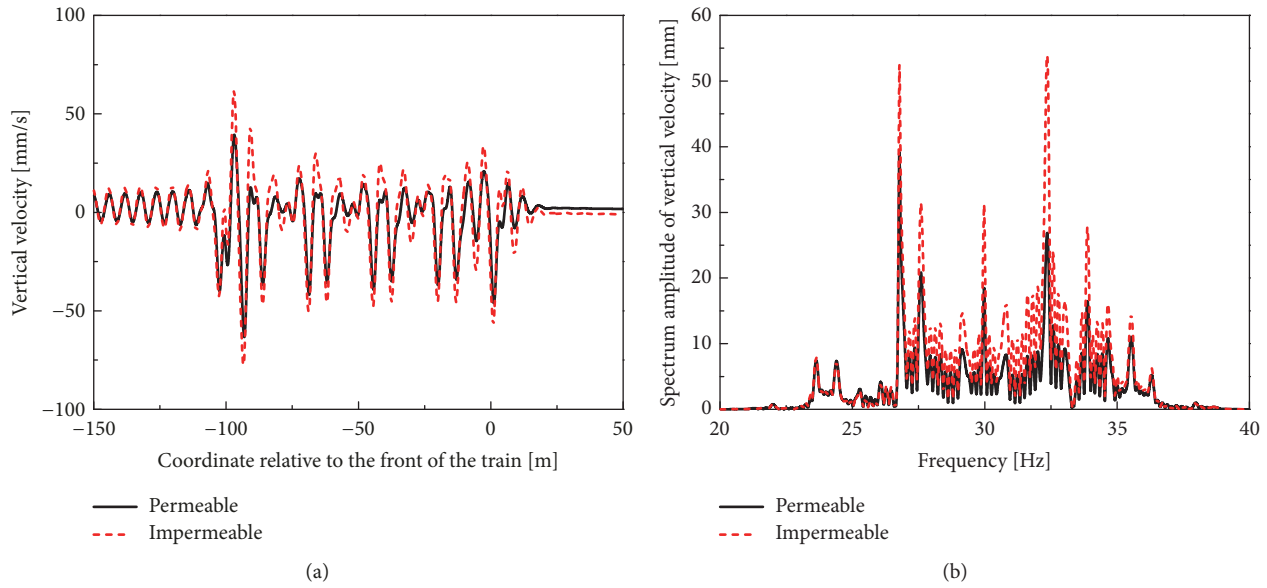


FIGURE 12: The vertical velocity under a moving train with $f_0 = 30$ Hz: (a) in the time domain and (b) in the frequency domain ($V = 70$ km/h).

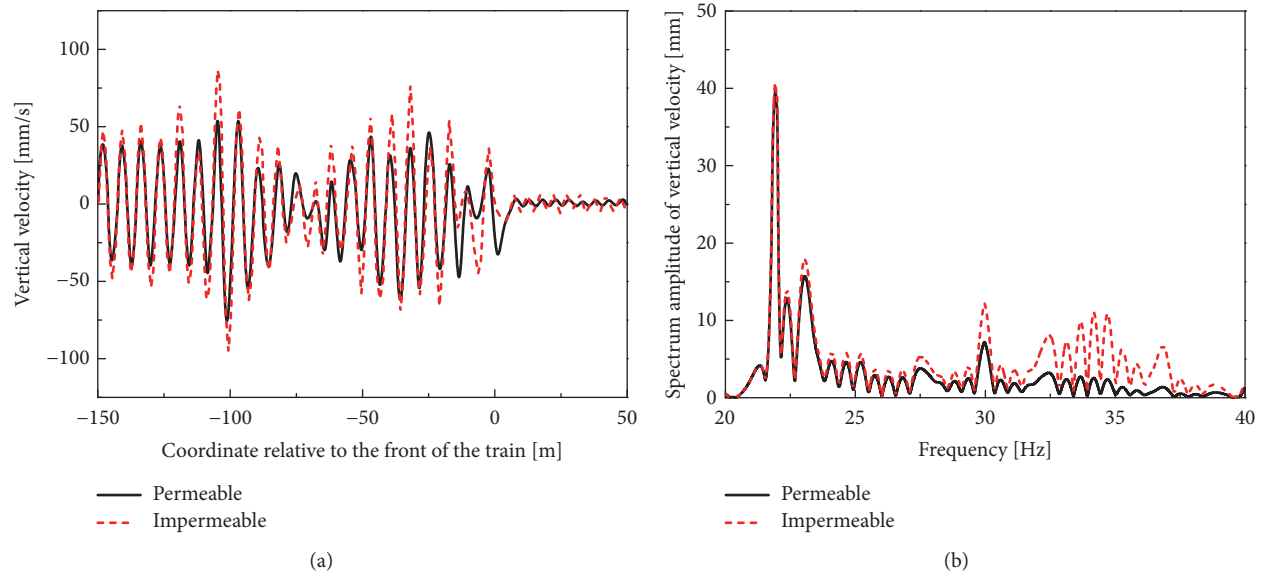


FIGURE 13: The vertical velocity under a moving train with $f_0 = 30$ Hz: (a) in the time domain and (b) in the frequency domain ($V = 250$ km/h).

soil permeability. The main conclusions of this paper are summarized as follows:

- (1) For moving trains with constant load amplitude, a critical velocity exists in the embankment-ground structure, which is larger than the shear wave velocity of the ground. The vertical velocity of the ground with permeable surface is much larger than that with impermeable surface when the train speed approaches the critical speed.
- (2) Considering the train loads as moving harmonic loads, the vertical velocity of the ground reaches a peak value at an excitation frequency around 10 Hz. The effect of the hydraulic boundary of the ground

surface on the vertical velocity response is limited at low load frequencies, while in the high frequency range the velocity response of the ground surface with impermeable boundary is significantly higher than that with permeable boundary.

- (3) The pore water pressure in the ground with impermeable surface is larger than that with permeable surface subjected to the moving train with a low self-excitation frequency. As the load frequency increases, the permeable surface will result in higher pore water pressure in the ground than the impermeable surface.
- (4) The hydraulic boundary effects on the ground vibration are significant when the soil permeability is

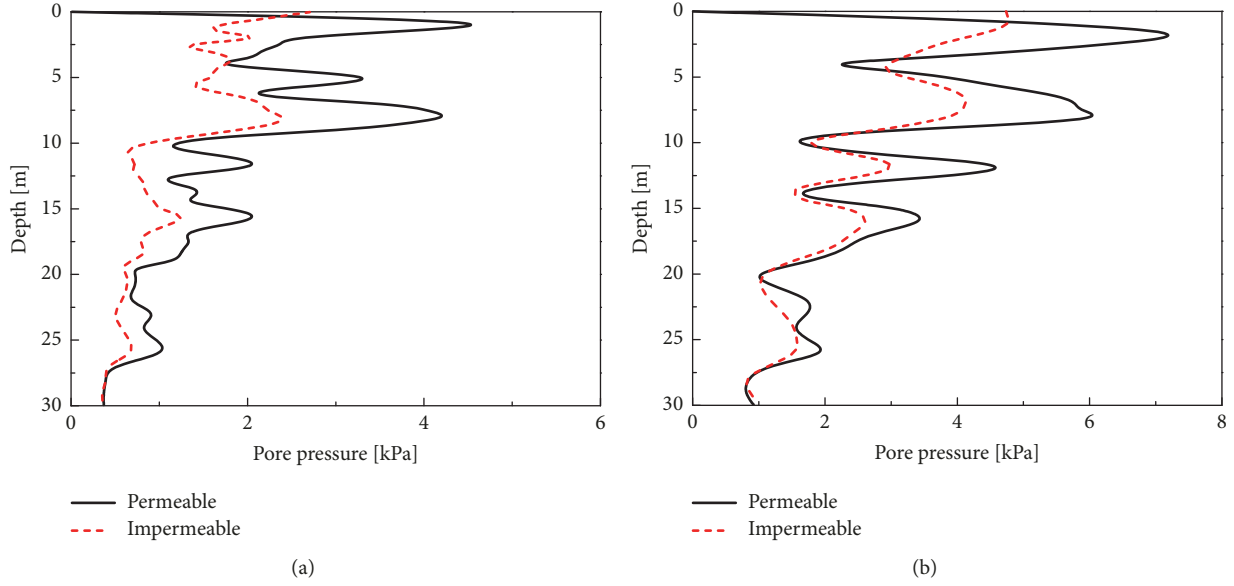


FIGURE 14: The maximum pore pressure under a moving train with $f_0 = 30$ Hz ($b = 1.0 \times 10^6$ N·s/m⁴): (a) $V = 70$ km/h and (b) $V = 250$ km/h.

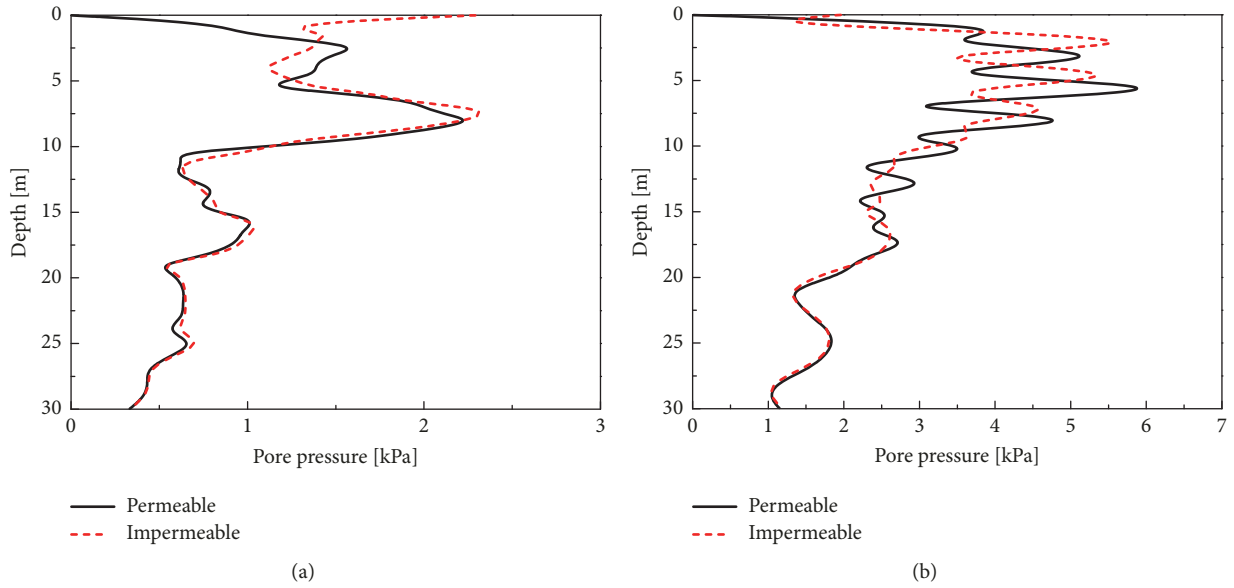


FIGURE 15: The maximum pore pressure under a moving train with $f_0 = 30$ Hz ($b = 1.0 \times 10^9$ N·s/m⁴): (a) $V = 70$ km/h and (b) $V = 250$ km/h.

high, while its effects are reduced when the soil permeability is decreased.

Appendix

$$\gamma_i = \sqrt{q^2 + p^2 - L_i^2}, \quad i = 1, 2 \quad (\text{A.1})$$

$$\gamma_3 = \sqrt{q^2 + p^2 + \frac{S^2}{\mu}} \quad (\text{A.2})$$

$$L_1^2 = \frac{\beta_1 + \sqrt{\beta_1^2 - 4\beta_2}}{2},$$

$$L_2^2 = \frac{\beta_1 - \sqrt{\beta_1^2 - 4\beta_2}}{2} \quad (\text{A.3})$$

$$S^2 = (\rho - \rho_f \vartheta) \omega^2 \quad (\text{A.4})$$

$$\beta_1 = \frac{(\lambda + 2\mu + \alpha^2 M)(m_1 \omega^2 - i b \omega) - 2\alpha M \rho_f \omega^2 + \rho M \omega^2}{(\lambda + 2\mu) M} \quad (\text{A.5})$$

$$\beta_2 = \frac{(m_1 \omega^2 - i b \omega) \rho \omega^2 - \rho_f^2 \omega^4}{(\lambda + 2\mu) M} \quad (\text{A.6})$$

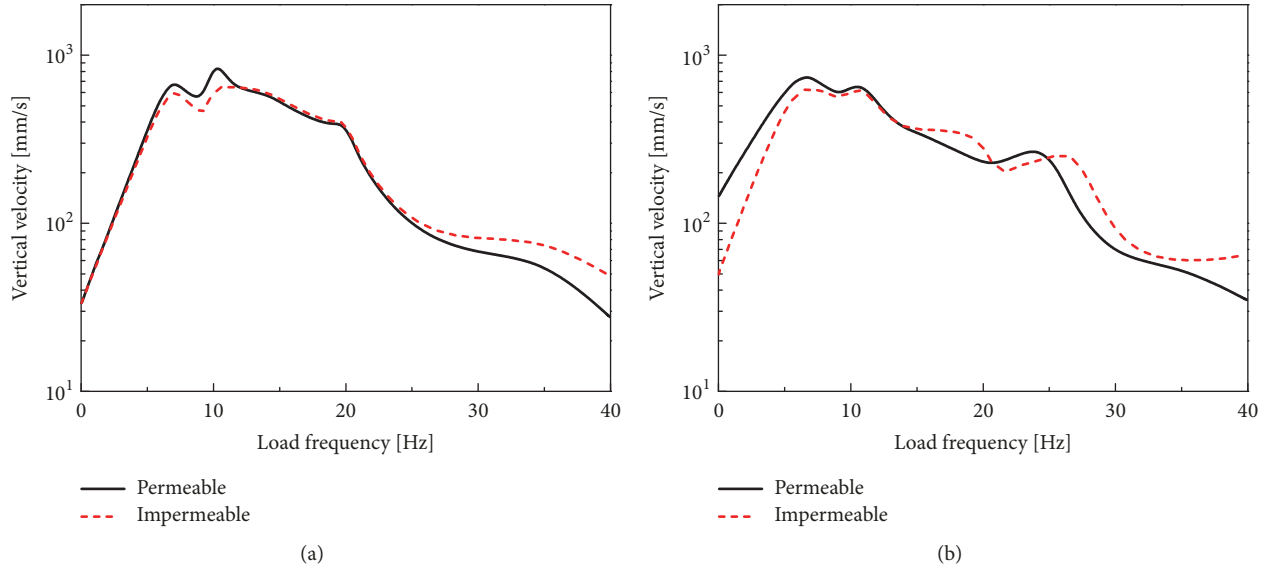


FIGURE 16: The vertical velocity versus the load frequency: (a) $V=70$ km/h and (b) $V=250$ km/h ($b=1.0 \times 10^6$ N·s/m⁴).

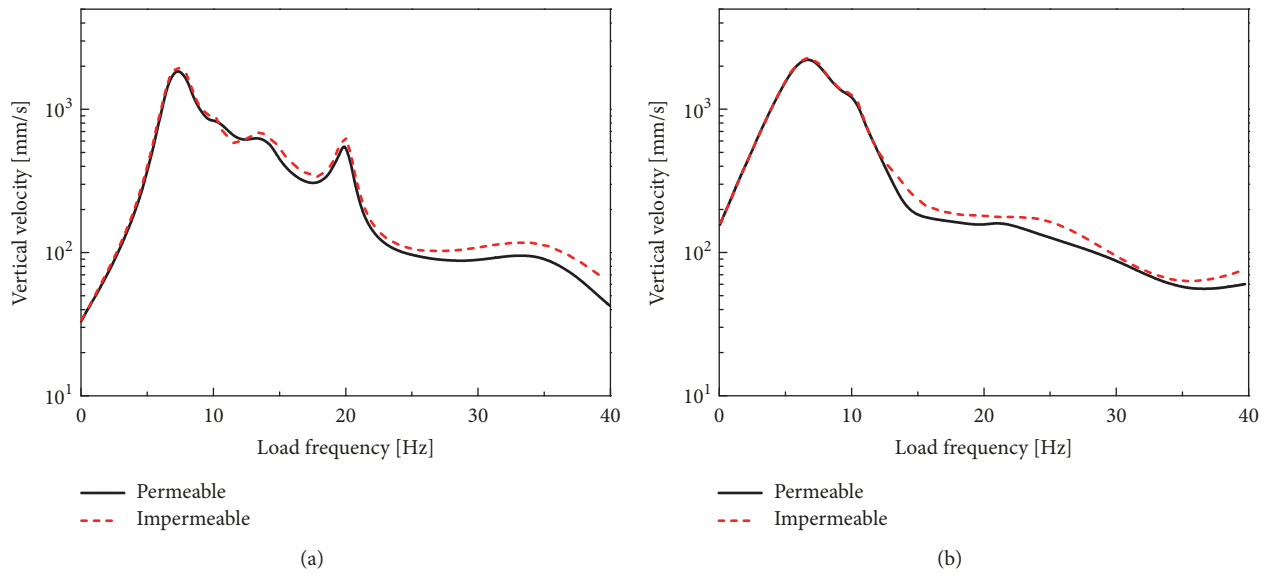


FIGURE 17: The vertical velocity versus the load frequency: (a) $V=70$ km/h and (b) $V=250$ km/h ($b=1.0 \times 10^9$ N·s/m⁴).

$$\chi_i = \frac{\vartheta ML_i^2 - \rho_f \omega^2}{\rho_f \omega^2 (\alpha - \vartheta) M} \quad i = 1, 2 \tag{A.7}$$

$$a_i = \frac{(\lambda + \mu) \chi_i - \alpha + \vartheta}{S^2 - \mu L_i^2} \quad i = 1, 2 \tag{A.8}$$

$$\vartheta = \frac{\rho_f \omega^2}{(m_1 \omega^2 - i b \omega)} \tag{A.9}$$

$$g_i = \chi_i + a_i (2q^2 - L_i^2) \quad i = 1, 2 \tag{A.10}$$

$$g_3 = \lambda \chi_1 - 2\mu \gamma_1^2 a_1 - \alpha, \tag{A.11}$$

$$g_4 = \lambda \chi_2 - 2\mu \gamma_2^2 a_2 - \alpha$$

Data Availability

No data were used to support this study.

Conflicts of Interest

The authors declare that there are no conflicts of interest regarding the publication of this paper.

Acknowledgments

This work is supported by the National Key Research and Development Plan of China (Grant No. 2016YFC0800204),

the National Natural Science Foundation of China (Grant Nos. 51578500 and 51708503), and the Natural Science Foundation of Zhejiang Province (Grant No. LY15E080009).

References

- [1] G. Eason, "The stresses produced in a semi-infinite solid by a moving surface force," *International Journal of Engineering Science*, vol. 2, no. 6, pp. 581–609, 1965.
- [2] R. Kumar and P. Ailawalia, "Moving load response of micropolar elastic half-space with voids," *Journal of Sound and Vibration*, vol. 280, no. 3-5, pp. 837–848, 2005.
- [3] Y. H. Huang, *Pavement Analysis and Design*, Prentice Hall, New Jersey, 1993.
- [4] A. V. Metrikine and H. A. Dieterman, "Lateral vibrations of an axially compressed beam on an elastic half-space due to a moving lateral load," *European Journal of Mechanics - A/Solids*, vol. 18, no. 1, pp. 147–158, 1999.
- [5] S. Kim, "Vibration and stability of axial loaded beams on elastic foundation under moving harmonic loads," *Engineering Structures*, vol. 26, no. 1, pp. 95–105, 2004.
- [6] S.-M. Kim, "Influence of horizontal resistance at plate bottom on vibration of plates on elastic foundation under moving loads," *Engineering Structures*, vol. 26, no. 4, pp. 519–529, 2004.
- [7] S. Lu, "Analytical dynamic displacement response of rigid pavements to moving concentrated and line loads," *International Journal of Solids and Structures*, vol. 43, no. 14-15, pp. 4370–4383, 2006.
- [8] X. Sheng, C. J. C. Jones, and D. J. Thompson, "A comparison of a theoretical model for quasi-statically and dynamically induced environmental vibration from trains with measurements," *Journal of Sound and Vibration*, vol. 267, no. 3, pp. 621–635, 2003.
- [9] X. Sheng, C. J. C. Jones, and D. J. Thompson, "A theoretical study on the influence of the track on train-induced ground vibration," *Journal of Sound and Vibration*, vol. 272, no. 3–5, pp. 909–936, 2004.
- [10] X. Sheng, C. J. C. Jones, and D. J. Thompson, "A theoretical model for ground vibration from trains generated by vertical track irregularities," *Journal of Sound and Vibration*, vol. 272, no. 3–5, pp. 937–965, 2004.
- [11] B. Picoux, R. Rotinat, J. P. Regoin, and D. Le Houédec, "Prediction and measurements of vibrations from a railway track lying on a peaty ground," *Journal of Sound and Vibration*, vol. 267, no. 3, pp. 575–589, 2003.
- [12] M. A. Biot, "Theory of propagation of elastic waves in a fluid-saturated porous solid. I. Low-frequency range," *The Journal of the Acoustical Society of America*, vol. 28, pp. 168–178, 1956.
- [13] R. Siddharthan, Z. Zafir, and G. M. Norris, "Moving load response of layered soil. I: Formulation," *Journal of Engineering Mechanics*, vol. 119, no. 10, pp. 2052–2071, 1993.
- [14] D. D. Theodorakopoulos, A. P. Chassiakos, and D. E. Beskos, "Dynamic effects of moving load on a poroelastic soil medium by an approximate method," *International Journal of Solids and Structures*, vol. 41, no. 7, pp. 1801–1822, 2004.
- [15] D. D. Theodorakopoulos, "Dynamic analysis of a poroelastic half-plane soil medium under moving loads," *Soil Dynamics and Earthquake Engineering*, vol. 23, no. 7, pp. 521–533, 2003.
- [16] B. Jin, "Dynamic responses of a poroelastic half space generated by high speed load," *Chinese Quarterly of Mechanics*, vol. 25, no. 2, pp. 168–174, 2004.
- [17] G.-B. Liu, P.-C. Wang, Y.-P. Chen, and H.-L. Yao, "Ground vibration of a finite layer of soft foundation in the vicinity of a moving load," *Yantu Lixue/Rock and Soil Mechanics*, vol. 27, no. 9, pp. 1607–1612, 2006.
- [18] B. Xu, J.-F. Lu, and J.-H. Wang, "Dynamic response of an infinite beam overlying a layered poroelastic half-space to moving loads," *Journal of Sound and Vibration*, vol. 306, no. 1-2, pp. 91–110, 2007.
- [19] G. Y. Gao, J. F. He, C. B. Yang et al., "Ground vibration induced by trains moving on saturated ground using 2.5D FEM," *Chinese Journal of Geotechnical Engineering*, vol. 33, no. 2, pp. 234–241, 2011.
- [20] F. Yu, Y.-S. Diao, X.-N. Tong, and Q.-L. Zhang, "Damage identification of an offshore platform based on curvature of modal shape difference and BP neural network," *Journal of Vibration and Shock*, vol. 30, no. 10, pp. 183–187, 2011.
- [21] K. Chahour, G. Lefeuvre-Mesgouez, and A. Mesgouez, "Spectral analysis of a railway track in contact with a multilayered poroviscoelastic soil subjected to a harmonic moving load," *Soil Dynamics and Earthquake Engineering*, vol. 64, pp. 24–37, 2014.
- [22] Y. Cai, Z. Cao, H. Sun, and C. Xu, "Effects of the dynamic wheel-rail interaction on the ground vibration generated by a moving train," *International Journal of Solids and Structures*, vol. 47, no. 17, pp. 2246–2259, 2010.
- [23] Z. G. Cao, Y. Q. Cai, H. L. Sun, and C. J. Xu, "Dynamic responses of a poroelastic half-space from moving trains caused by vertical track irregularities," *International Journal for Numerical and Analytical Methods in Geomechanics*, vol. 35, no. 7, pp. 761–786, 2011.
- [24] S. Zhou, C. He, and H. Di, "Dynamic 2.5-D Green's function for a poroelastic half-space," *Engineering Analysis with Boundary Elements*, vol. 67, pp. 96–107, 2016.
- [25] A. Karlström and A. Boström, "An analytical model for train-induced ground vibrations from railways," *Journal of Sound and Vibration*, vol. 292, no. 1-2, pp. 221–241, 2006.
- [26] C. Madshus and A. M. Kaynia, "High-speed railway lines on soft ground: dynamic behaviour at critical train speed," *Journal of Sound and Vibration*, vol. 231, no. 3, pp. 689–701, 2000.
- [27] Z. Yuan, A. Boström, Y. Cai, and Z. Cao, "Analytical solution for calculating vibrations from twin circular tunnels," *Soil Dynamics and Earthquake Engineering*, vol. 117, pp. 312–327, 2019.
- [28] Z. Cao and A. Boström, "Dynamic response of a poroelastic half-space to accelerating or decelerating trains," *Journal of Sound and Vibration*, vol. 332, no. 11, pp. 2777–2794, 2013.



Hindawi

Submit your manuscripts at
www.hindawi.com

